



High-temperature transport properties, thermal expansion and cathodic performance of Ni-substituted $\text{LaSr}_2\text{Mn}_2\text{O}_{7-\delta}$

A.A. Yaremchenko^a, D.O. Bannikov^{a,b}, A.V. Kovalevsky^{a,c}, V.A. Cherepanov^b, V.V. Kharton^{a,*}

^a Department of Ceramics and Glass Engineering, CICECO, University of Aveiro, 3810-193 Aveiro, Portugal

^b Department of Chemistry, Ural State University, Lenin av. 51, Ekaterinburg 620083, Russia

^c Materials Department, Flemish Institute for Technological Research (VITO), 2400 Mol, Belgium

ARTICLE INFO

Article history:

Received 22 May 2008

Received in revised form

18 July 2008

Accepted 24 July 2008

Available online 9 August 2008

Keywords:

Ruddlesden–popper manganite

Mixed conductor

Oxygen permeability

Solid oxide fuel cell cathode

Seebeck coefficient

Thermal expansion

ABSTRACT

The substitution of manganese with nickel in $\text{LaSr}_2\text{Mn}_2\text{O}_{7-\delta}$, where the solubility limit corresponds to approximately 25% Mn sites, enhances the Ruddlesden–Popper phase stability at elevated temperatures and atmospheric oxygen pressure. The total conductivity of $\text{LaSr}_2\text{Mn}_{2-y}\text{Ni}_y\text{O}_{7-\delta}$ ($y = 0-0.4$) decreases with nickel additions, whilst the average thermal expansion coefficients calculated from dilatometric data in the temperature range 300–1370 K increase from $(11.4-13.7) \times 10^{-6} \text{K}^{-1}$ at $y = 0$ up to $(12.5-14.4) \times 10^{-6} \text{K}^{-1}$ at $y = 0.4$. The conductivity and Seebeck coefficient of $\text{LaSr}_2\text{Mn}_{1.6}\text{Ni}_{0.4}\text{O}_{7-\delta}$, analyzed in the oxygen partial pressure range $10^{-15}-0.3$ atm at 600–1270 K, display that the electronic transport is n-type and occurs via a small polaron mechanism. Reductive decomposition is observed at the oxygen pressures close to Ni/NiO boundary, namely $\sim 2.3 \times 10^{-11}$ atm at 1223 K. Within the phase stability domain, the electronic transport properties are essentially $p(\text{O}_2)$ -independent. The steady-state oxygen permeability of dense $\text{LaSr}_2\text{Mn}_{1.6}\text{Ni}_{0.4}\text{O}_{7-\delta}$ membranes is higher than that of $(\text{La,Sr})\text{MnO}_{3-\delta}$, but lower if compared to perovskite-like $(\text{Sr,Ce})\text{MnO}_{3-\delta}$. Porous $\text{LaSr}_2\text{Mn}_{1.6}\text{Ni}_{0.4}\text{O}_{7-\delta}$ cathodes in contact with apatite-type $\text{La}_{10}\text{Si}_5\text{AlO}_{26.5}$ solid electrolyte exhibit, however, a relatively poor electrochemical performance, partly associated with strong cation interdiffusion between the materials.

© 2008 Elsevier Inc. All rights reserved.

1. Introduction

Manganese-based Ruddlesden–Popper (RP) phases possess an attractive combination of structural, magnetic and electrical properties, including the colossal magnetoresistance (CMR) effect [1–15]. One potential application of these materials relates also to porous cathodes of solid oxide fuel cells (SOFCs), the alternative power generation systems enabling to increase energy conversion efficiency. Several RP manganites and nickelates were evaluated recently for possible use in the intermediate-temperature SOFCs operating at 870–1070 K [5,16]; the higher-order RP phases, with general formula $\text{A}_{n+1}\text{B}_n\text{O}_{3n+1}$ where $n = 2$ or 3, were suggested as promising cathode materials [16].

This work is focused on synthesis and characterization of $\text{LaSr}_2\text{Mn}_{2-y}\text{Ni}_y\text{O}_{7-\delta}$ system at elevated temperatures necessary for the fuel cell fabrication and operation. The parent compound, $\text{LaSr}_2\text{Mn}_2\text{O}_7$, has a layered $n = 2$ RP structure which can be described as a succession of perovskite bilayers alternating with rock-salt $(\text{La,Sr})\text{O}$ sheets along the crystallographic c -axis. Since the first observations of CMR in bilayered manganites in 1990s [1], the crystal chemistry, electrical and magnetic properties of

$\text{LaSr}_2\text{Mn}_2\text{O}_7$ and related oxide systems, $\text{La}_{2-2x}\text{Sr}_{1+2x}\text{Mn}_{2-y}\text{B}_y\text{O}_{7-\delta}$ (B —transition metal cation), were extensively studied at temperatures below 350 K (e.g. [6–15] and references cited). Information on the high-temperature properties of these materials is, however, almost absent. $\text{LaSr}_2\text{Mn}_2\text{O}_7$ was reported to be nearly oxygen-stoichiometric in air [10]. Due to equal concentrations of Mn^{3+} and Mn^{4+} cations, a highest conductivity level in the $\text{La}_{2-2x}\text{Sr}_{1+2x}\text{Mn}_2\text{O}_{7-\delta}$ family can be expected for this compound. As the solubility of strontium and manganese cations in the corresponding sublattices of $\text{La}_3\text{Ni}_2\text{O}_{7-\delta}$ is very low [17,18], the present study was centered on the Mn-rich part of $\text{LaSr}_2\text{Mn}_{2-y}\text{Ni}_y\text{O}_{7-\delta}$ system. Taking into account the superior electrode behavior of numerous RP nickelates (e.g. [5]), doping of $\text{LaSr}_2\text{Mn}_2\text{O}_7$ with nickel might be expected to enhance the oxygen-ionic transport and electrochemical activity. Attention was also focused on other properties relevant for potential applications in SOFC cathodes, including the electronic conduction, thermal expansion and phase stability. The cathodic performance of porous electrodes was evaluated in contact with $\text{La}_{10}\text{Si}_5\text{AlO}_{26.5}$ solid electrolyte [19]. The ionic conductors based on apatite-type $\text{La}_{10-x}(\text{SiO}_4)_6\text{O}_{2\pm\delta}$ may provide serious advantages for the intermediate-temperature SOFCs owing to a substantially high oxygen diffusivity and relatively low costs [20]; however, data on their behavior in high-temperature electrochemical cells are still scarce.

* Corresponding author. Fax: +351 234 425300.

E-mail address: kharton@ua.pt (V.V. Kharton).

2. Experimental

Submicron powders of $\text{LaSr}_2\text{Mn}_{2-y}\text{Ni}_y\text{O}_{7-\delta}$ ($y = 0-0.6$) were prepared by the glycine-nitrate process (GNP), a self-combustion technique using metal nitrates as oxidant and glycine as a fuel and chelating agent [21]. In the course of GNP, aqueous glycine-nitrate solutions containing metal cations in the stoichiometric proportions were dried and heated until auto-ignition. The foam-like products were ground, annealed in air at 1173 K for 2 h in order to remove organic residues, and then ball-milled. Ceramic samples were pressed uniaxially at 350–400 MPa and sintered in air at 1673–1823 K for 10–40 h. After sintering and polishing, all materials were annealed at 1273 K for 2 h and slowly (1–2 K/min) cooled down to room temperature in order to achieve equilibrium with atmospheric oxygen. X-ray diffraction (XRD) patterns were recorded on a Rigaku D/MAX-B diffractometer ($\text{CuK}\alpha$, $2\theta = 10-100^\circ$, step 0.02°). A Hitachi S-4100 scanning electron microscope (SEM) with a Rontec UHV detection system for the energy dispersive spectroscopy (EDS) was used for microstructural studies. Thermogravimetric analysis (TGA, Setaram SetSys 16/18) was performed in a flow of dried air in continuous heating/cooling regime (2 K/min). The dilatometric studies were carried out using a vertical Linseis L75 instrument (accuracy $\pm 2 \mu\text{m}$, sample length of 10–12 mm) in air. General characterization of the ceramic materials included also determination of steady-state oxygen permeation fluxes (j) as function of temperature and oxygen partial pressure gradient, and measurements of the total conductivity (σ , 4-probe DC) and Seebeck coefficient (α). The equipment and experimental procedures used for materials characterization were described elsewhere ([19,22,23] and references therein). The electrical properties were studied at 600–1270 K in the oxygen partial pressure range 10^{-15} –0.3 atm; the criteria for equilibration after a change in either oxygen pressure or temperature included the relaxation rates of the conductivity and Seebeck coefficient less than 0.05%/min and $0.001 \mu\text{V}/(\text{K min})$, respectively. The investigations of steady-state electrode polarization were carried out by the 3-electrode technique in cells with symmetrical working and counter electrodes (WE and CE); the cell geometry was selected according to Ref. [24]. The porous WEs (sheet density of $18.4 \text{ mg}/\text{cm}^2$) were made of single-phase $\text{LaSr}_2\text{Mn}_{1.6}\text{Ni}_{0.4}\text{O}_{7-\delta}$ powder annealed in air at 1423–1593 K for 40 h with several intermediate milling steps; the powder was suspended in ethanol and deposited onto dense $\text{La}_{10}\text{Si}_5\text{AlO}_{26.5}$ substrates, followed by the final annealing step at 1503 K for 2 h. The counter and reference electrodes, both made of porous Pt, were sintered at 1273 K for 0.5 h. The processing conditions of $\text{La}_{10}\text{Si}_5\text{AlO}_{26.5}$ electrolyte ceramics were described elsewhere [19]. The polarization experiments were performed in the galvanostatic mode using an AUTOLAB PGSTAT302 instrument at 873–1073 K in atmospheric air. The values of the ohmic and polarization resistances were determined from the impedance spectra collected in the frequency range from 10 mHz to 1 MHz; the relaxation times after a change in the WE potential were 30–70 min. The phase composition and microstructure of the electrode layers before and after electrochemical measurements were examined by XRD and SEM/EDS.

3. Results and discussion

XRD analysis of $\text{LaSr}_2\text{Mn}_{2-y}\text{Ni}_y\text{O}_{7-\delta}$ ($y = 0-0.4$) ceramics sintered at 1773 K in air, showed the formation of tetragonal $\text{Sr}_3\text{Ti}_2\text{O}_7$ -type structure (Figs. 1A, D and 2A). However, whilst $\text{LaSr}_2\text{Mn}_{1.6}\text{Ni}_{0.4}\text{O}_{7-\delta}$ is single-phase, XRD patterns of $\text{LaSr}_2\text{Mn}_{2-y}\text{Ni}_y\text{O}_{7-\delta}$ ($y = 0-0.2$) indicate the presence of secondary perovskite-type component. Longer sintering time at this

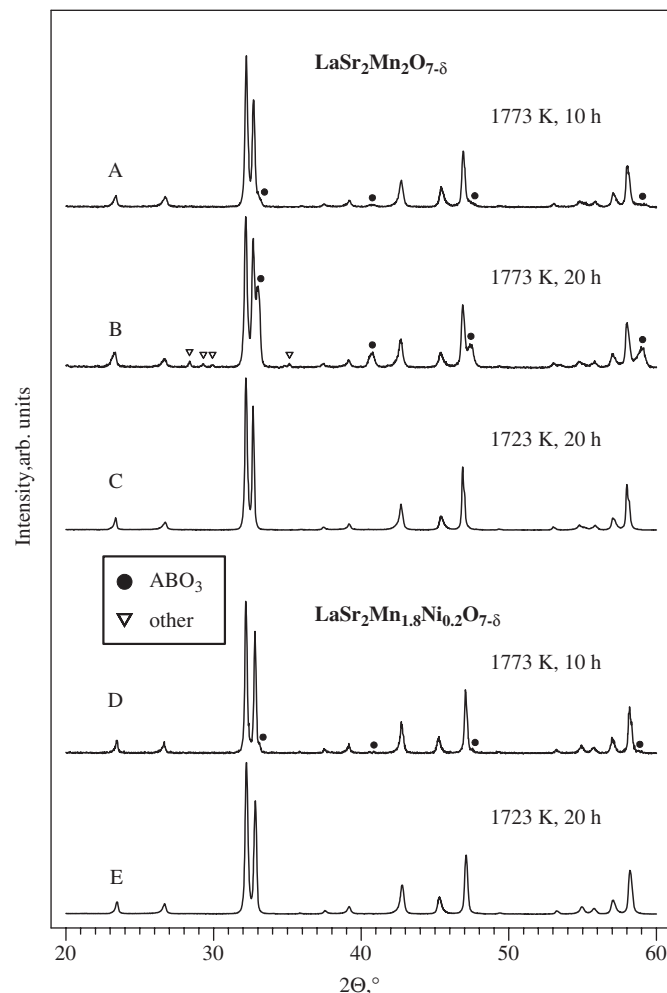


Fig. 1. XRD patterns of $\text{LaSr}_2\text{Mn}_2\text{O}_{7-\delta}$ (A–C) and $\text{LaSr}_2\text{Mn}_{1.8}\text{Ni}_{0.2}\text{O}_{7-\delta}$ (D and E) ceramics sintered under different conditions.

temperature resulted only in a larger fraction of the perovskite phase impurity, as illustrated by Fig. 1B. Single-phase $\text{LaSr}_2\text{Mn}_2\text{O}_{7-\delta}$ and $\text{LaSr}_2\text{Mn}_{1.8}\text{Ni}_{0.2}\text{O}_{7-\delta}$ ceramics were only obtained after sintering at lower temperatures, such as 1723 K (Figs. 1C and E), insufficient to achieve density higher than 90% (Table 1). Attempts to prepare single-phase $\text{LaSr}_2\text{Mn}_{1.4}\text{Ni}_{0.6}\text{O}_{7-\delta}$ failed. The samples of this composition comprise a major perovskite phase after sintering at 1823 K (Fig. 2C), and melt at 1873 K. In addition to the $\text{Sr}_3\text{Ti}_2\text{O}_7$ -type solid solution, $\text{LaSr}_2\text{Mn}_{1.4}\text{Ni}_{0.6}\text{O}_{7-\delta}$ ceramics sintered at 1673–1773 K comprise also a K_2NiF_4 -type phase impurity (Figs. 2D–F); increasing the duration of thermal treatment has rather a negligible effect on the intensity of secondary phase reflections. Therefore, the solubility limit of nickel cations in $\text{LaSr}_2\text{Mn}_2\text{O}_{7-\delta}$ at atmospheric oxygen pressure corresponds to approximately 25% manganese sites.

The crystal structure of $\text{LaSr}_2\text{Mn}_{2-y}\text{Ni}_y\text{O}_{7-\delta}$ ($y = 0-0.4$) was refined in $I4/mmm$ space group. The substitution of manganese with nickel leads to a lattice contraction along the ab planes and to an expansion along the c -axis (Table 1). As a result, the unit cell volume decreases on doping. Due to an enhanced thermodynamic stability of the $n = 2$ RP phase containing 20% Ni at elevated temperatures which makes it possible to sinter gas-tight ceramic materials with density higher than 95% in air (Table 1), the maximum attention in this work was focused on $\text{LaSr}_2\text{Mn}_{1.6}\text{Ni}_{0.4}\text{O}_{7-\delta}$.

The dilatometric curves of $\text{LaSr}_2\text{Mn}_{2-y}\text{Ni}_y\text{O}_{7-\delta}$ ceramics in air are almost linear, but exhibit a tendency to increasing thermal expansion coefficients (TECs, $\bar{\alpha}$) when temperature increases (Fig. 3). The average TECs vary from $(11.4\text{--}12.5) \times 10^{-6} \text{K}^{-1}$ at 300–900 K up to $(13.7\text{--}14.4) \times 10^{-6} \text{K}^{-1}$ at 900–1370 K (Table 2). Doping with nickel also leads to moderately higher thermal expansion which remains, however, still compatible with that of

solid oxide electrolytes [20]. As there was no evidence of structural changes in the studied temperature range, the modest non-linearity of the RP lattice expansion might be associated with so-called chemical contribution originating from progressive oxygen losses on heating and the corresponding reduction of the transition metal cations, increasing their radii. At the same time, the variations of the oxygen content in $\text{LaSr}_2\text{Mn}_{1.6}\text{Ni}_{0.4}\text{O}_{7-\delta}$ at 570–1370 K are less than 0.015 atoms per formula unit at atmospheric oxygen pressure (Fig. 4). This suggests that the increase in TECs should be contributed by parallel inter-related processes in the manganese sublattice, such as thermally induced Mn^{3+} disproportionation and shifting the equilibrium between $\text{Mn}^{3+}/\text{Mn}^{4+}$ and $\text{Ni}^{2+}/\text{Ni}^{3+}$ redox couples on heating, and/or by increasing anharmonicity of the atomic vibrations on doping. The low variations of Seebeck coefficient with temperature and the conductivity behavior, discussed below, may argue in favor

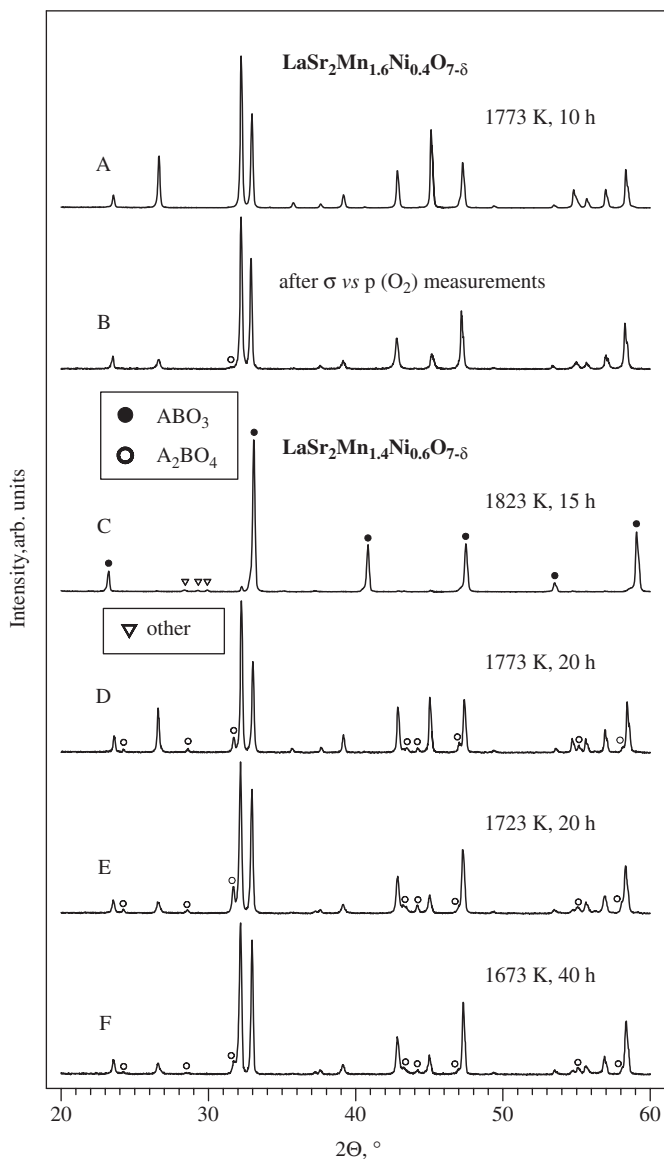


Fig. 2. XRD patterns of as-prepared $\text{LaSr}_2\text{Mn}_{1.6}\text{Ni}_{0.4}\text{O}_{7-\delta}$ (A) and $\text{LaSr}_2\text{Mn}_{1.4}\text{Ni}_{0.6}\text{O}_{7-\delta}$ (C–F) ceramics sintered under different conditions, and $\text{LaSr}_2\text{Mn}_{1.6}\text{Ni}_{0.4}\text{O}_{7-\delta}$ ceramics after the measurements of electrical properties in reducing atmospheres and subsequent re-oxidation (B).

Table 1
Density and unit cell parameters of $\text{LaSr}_2\text{Mn}_{2-y}\text{Ni}_y\text{O}_{7-\delta}$ ceramics

Composition	Sintering conditions	ρ_{exp} ($\text{g} \times \text{cm}^{-3}$)	$\rho_{\text{exp}}/\rho_{\text{theor}}$ (%)	Unit cell parameters		
				a (\AA)	c (\AA)	V (\AA^3)
$\text{LaSr}_2\text{Mn}_2\text{O}_{7-\delta}$	1723 K/20 h	3.92	66.3	3.878(1)	20.004(27)	300.8(6)
$\text{LaSr}_2\text{Mn}_{1.8}\text{Ni}_{0.2}\text{O}_{7-\delta}$	1723 K/20 h	4.95	83.1	3.864(1)	20.060(29)	299.6(6)
$\text{LaSr}_2\text{Mn}_{1.6}\text{Ni}_{0.4}\text{O}_{7-\delta}$	1773 K/10 h	5.70	95.1	3.8502(1)	20.1134(6)	298.17(2)

Note: ρ_{exp} and ρ_{theor} are the experimental density and theoretical density calculated from the XRD data, respectively.

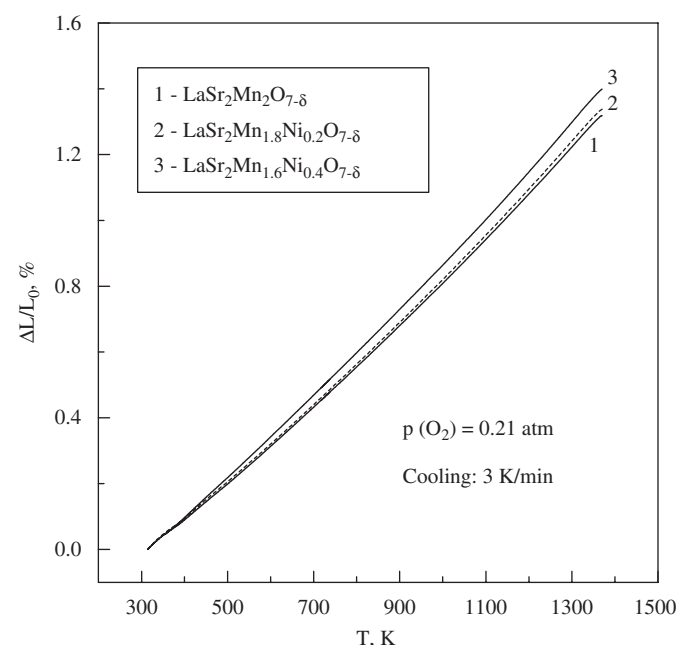


Fig. 3. Dilatometric curves of $\text{LaSr}_2\text{Mn}_{2-y}\text{Ni}_y\text{O}_{7-\delta}$ ceramics in air.

Table 2
Average TECs and activation energy for the total conductivity of $\text{LaSr}_2\text{Mn}_{2-y}\text{Ni}_y\text{O}_{7-\delta}$ ceramics in air

Composition	Average linear TECs ($\bar{\alpha} \pm 0.02$) $\times 10^6$ (K^{-1})		Activation energy for total conductivity E_A (kJ/mol) (600–1270 K)
	300–900 K	900–1370 K	
$\text{LaSr}_2\text{Mn}_2\text{O}_{7-\delta}$	11.42	13.72	17.1 ± 0.2
$\text{LaSr}_2\text{Mn}_{1.8}\text{Ni}_{0.2}\text{O}_{7-\delta}$	11.55	13.92	18.5 ± 0.1
$\text{LaSr}_2\text{Mn}_{1.6}\text{Ni}_{0.4}\text{O}_{7-\delta}$	12.47	14.35	18.2 ± 0.3

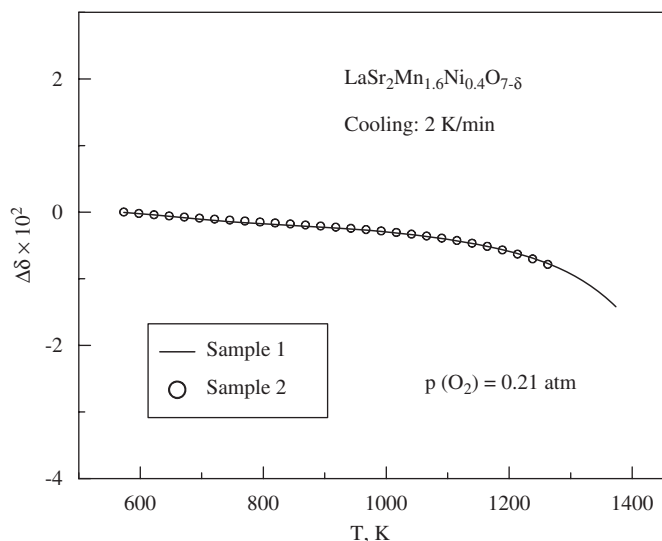


Fig. 4. Relative variations of the oxygen nonstoichiometry of $\text{LaSr}_2\text{Mn}_{1.6}\text{Ni}_{0.4}\text{O}_{7-\delta}$ in air, calculated from the thermogravimetric data.

of the latter hypothesis. Whatever the microscopic mechanisms, the average TECs of $\text{LaSr}_2\text{Mn}_{2-y}\text{Ni}_y\text{O}_{7-\delta}$ are quite similar to that of perovskite-type $\text{La}_{0.5}\text{Sr}_{0.5}\text{MnO}_{3-\delta}$ ($\bar{\alpha} = 12.3 \times 10^{-6} \text{ K}^{-1}$ at 320–1100 K [25]), but are lower compared to K_2NiF_4 -type $\text{La}_{0.6}\text{Sr}_{1.4}\text{MnO}_{4\pm\delta}$ ($\bar{\alpha} = 15.1 \times 10^{-6} \text{ K}^{-1}$ at 300–1073 K [5]). Hence, in contrast to the nickelate- and ferrite-based RP families [26], increasing the number of rock-salt layers in the RP-type manganites seems to increase their thermal expansion.

The total conductivity of $\text{LaSr}_2\text{Mn}_{2-y}\text{Ni}_y\text{O}_{7-\delta}$ displays a thermally activated character in the entire temperature range studied in this work, 600–1270 K (Fig. 5). The transport is predominantly electronic; the oxygen-ion transference numbers of $\text{LaSr}_2\text{Mn}_{1.6}\text{Ni}_{0.4}\text{O}_{7-\delta}$, estimated from the oxygen permeation data discussed below, are lower than 2×10^{-5} at 1248 K and decrease on cooling. As expected, the conductivity values of all single-phase $\text{LaSr}_2\text{Mn}_{2-y}\text{Ni}_y\text{O}_{7-\delta}$ ceramics are substantially higher compared to $\text{La}_{0.4}\text{Sr}_{1.6}\text{MnO}_{4\pm\delta}$, an $n = 1$ RP phase having maximum conductivity in $\text{La}_{2-x}\text{Sr}_x\text{MnO}_{4\pm\delta}$ series at 650–1000 K [5].

Although the conductivity of $\text{LaSr}_2\text{Mn}_2\text{O}_{7-\delta}$ and $\text{LaSr}_2\text{Mn}_{1.8}\text{Ni}_{0.2}\text{O}_{7-\delta}$ appears undervalued due to high porosity (Table 1), the results clearly show that Ni doping decreases electronic transport. The activation energies are, however, similar for all title materials (Table 2), suggesting that the conduction mechanism remains essentially unchanged. Note that substantially better electrical properties were reported for highly porous $\text{La}_{n+1}\text{Ni}_n\text{O}_{3n+1}$ ($n = 2, 3$) with the ceramics density as low as 54% [16] (Fig. 5). Such a difference may indicate that nickel cations provide no significant contribution to the electronic transport in $\text{LaSr}_2\text{Mn}_{2-y}\text{Ni}_y\text{O}_{7-\delta}$, but rather act as charge-carrier traps. A higher conductivity might be therefore expected if the nickel content would be above the critical percolation limit. For a cubic lattice with random cation distribution, this threshold corresponds to approximately 31% fraction [27,28]. In the case of bilayered $\text{LaSr}_2\text{Mn}_{2-y}\text{Ni}_y\text{O}_{7-\delta}$ where each Mn-site cation has only five nearest neighbors, the nickel percolation threshold should be higher and is beyond the solid solution domain. It should also be mentioned that the electrical resistivity in other $\text{La}_{2-2x}\text{Sr}_{1+2x}\text{Mn}_{2-y}\text{B}_y\text{O}_{7-\delta}$ ($B = \text{Cu, Co, Fe, Cr or Ti}$) systems at temperatures below 350 K increases on doping [11–15], a result of breaking $\text{Mn}^{4+}-\text{O}^{2-}-\text{Mn}^{3+}$ chains and, consequently, hampered electronic transfer which occurs via the so-called double-exchange interaction mechanism between manganese cations.

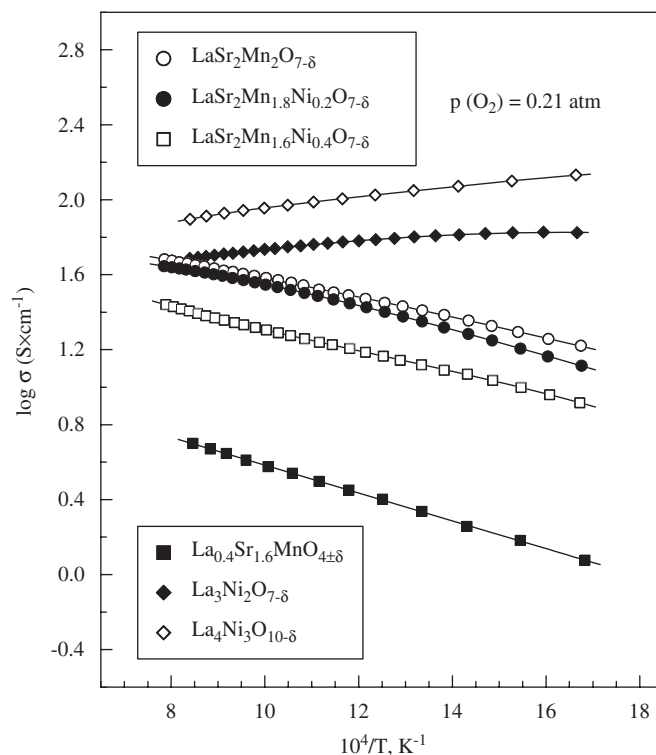


Fig. 5. Total conductivity of $\text{LaSr}_2\text{Mn}_{2-y}\text{Ni}_y\text{O}_{7-\delta}$ ceramics in air. Literature data on $\text{La}_{0.4}\text{Sr}_{1.6}\text{MnO}_{4\pm\delta}$ [5], and porous $\text{La}_3\text{Ni}_2\text{O}_{7-\delta}$ and $\text{La}_4\text{Ni}_3\text{O}_{10-\delta}$ with $\sim 54\%$ density [16] are shown for comparison.

The total conductivity and Seebeck coefficient of $\text{LaSr}_2\text{Mn}_{1.6}\text{Ni}_{0.4}\text{O}_{7-\delta}$ are essentially $p(\text{O}_2)$ -independent at 973–1223 K under oxidizing conditions, when the oxygen partial pressure is above 10^{-5} atm (Fig. 6). Also, the Seebeck coefficient is almost constant at fixed $p(\text{O}_2)$ (Fig. 7A). These trends reflect very minor changes of the oxygen nonstoichiometry at $p(\text{O}_2)$ values close to atmospheric conditions, in agreement with thermogravimetric data (Fig. 4). The negative sign of thermopower indicates that the electronic transport is n-type. Neglecting the transported heat of electrons and spin degeneracy phenomena, the Seebeck coefficient can be expressed by Heikes formula [29]:

$$\alpha = -\frac{k}{e} \ln\left(\frac{N-n}{n}\right) \quad (1)$$

where n and N are the concentration of electrons and the number of states, respectively. The n/N ratio estimated from the Seebeck coefficient data is 0.28–0.29 under oxidizing conditions (Fig. 7A). This value confirms that the conduction involves $\text{Mn}^{3+}/\text{Mn}^{4+}$ pairs where Mn^{3+} can be considered as the electronic charge carriers localized on manganese cations, whereas $\text{Ni}^{2+}/\text{Ni}^{3+}$ ions are essentially excluded from the transport processes; analysis of the relevant mechanisms can be found in literature (e.g., see [11–15] and references cited). The electron mobility (μ_n) calculated assuming that the electronic conductivity is governed exclusively by manganese cations, exhibits a temperature-activated character with values typical for small polaron conductors, 0.040–0.055 $\text{cm}^2/\text{s V}$ at 973–1223 K (Fig. 7B).

The electrical properties of $\text{LaSr}_2\text{Mn}_{1.6}\text{Ni}_{0.4}\text{O}_{7-\delta}$ in moderately reducing conditions remain almost unchanged down to oxygen pressures as low as 10^{-10} atm at 1223 K (Fig. 8). Further reduction leads to a slow decrease of the conductivity and to an increase of thermopower, followed by abrupt conductivity drop below 10^{-12} atm. Subsequent re-oxidation is accompanied with a large

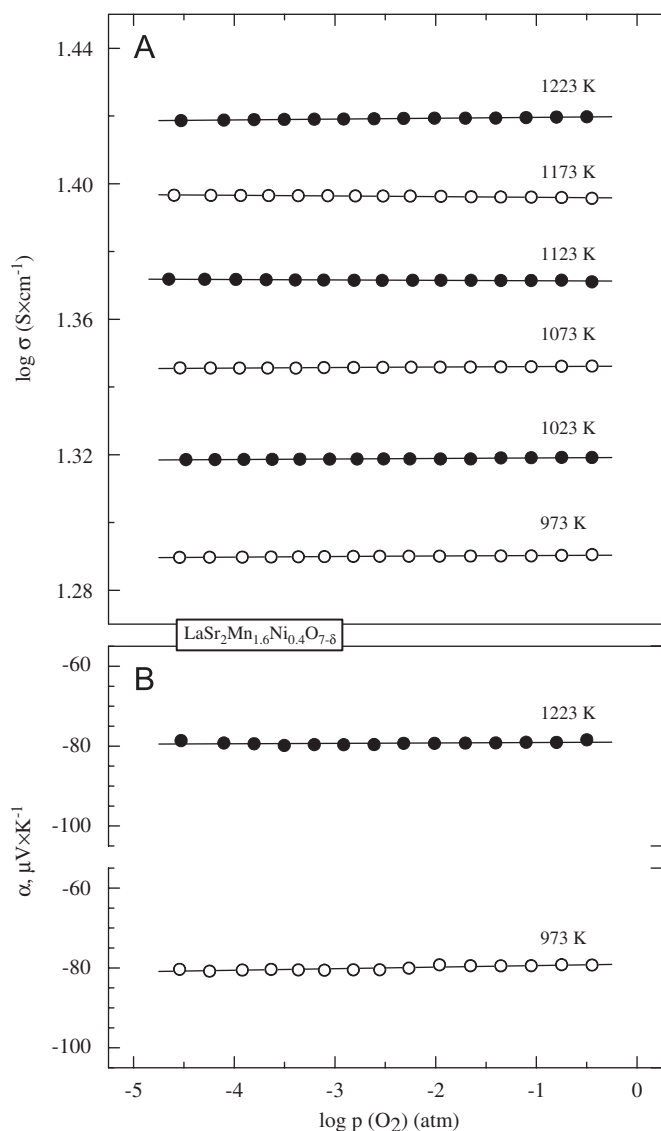


Fig. 6. Oxygen partial pressure dependence of the total conductivity (A) and Seebeck coefficient (B) of $\text{LaSr}_2\text{Mn}_{1.6}\text{Ni}_{0.4}\text{O}_{7-\delta}$ under oxidizing conditions.

hysteresis with two transitions visible in the σ vs. $p(\text{O}_2)$ and α vs. $p(\text{O}_2)$ curves; the initial values of conductivity and Seebeck coefficient cannot be reproduced after re-oxidation during 30–50 h. XRD inspection showed the appearance of small impurity peaks assigned to K_2NiF_4 -type phase (Fig. 2B). The drastic decrease in the total conductivity results, hence, from phase decomposition occurring via separation of the $n = 1$ RP compound, as for $\text{La}_3\text{Ni}_2\text{O}_7$ [30]. The oxygen partial pressure, at which the electrical properties start to deviate from the plateau-like behavior, was considered as an approximate stability limit at the given temperature. The phase stability boundary of $\text{LaSr}_2\text{Mn}_{1.6}\text{Ni}_{0.4}\text{O}_{7-\delta}$ corresponds to higher oxygen chemical potentials if compared to $(\text{La,Sr})\text{MnO}_{3-\delta}$, and is similar to that of NiO (Table 3). At the same time, the reduction of Mn_3O_4 into MnO occurs at still higher $p(\text{O}_2)$ values. The decomposition of $\text{LaSr}_2\text{Mn}_{1.6}\text{Ni}_{0.4}\text{O}_{7-\delta}$ is hence related to changing manganese and nickel oxidation state at the initial stage; increasing oxygen deficiency and formation of substantial amounts of Mn^{2+} and Ni^{2+} result in excessive stress in the lattice and collapse of the $n = 2$ RP structure, followed by nickel reduction into metal.

Selected results on the oxygen permeability of dense $\text{LaSr}_2\text{Mn}_{1.6}\text{Ni}_{0.4}\text{O}_{7-\delta}$ membranes are presented in Figs. 9 and 10.

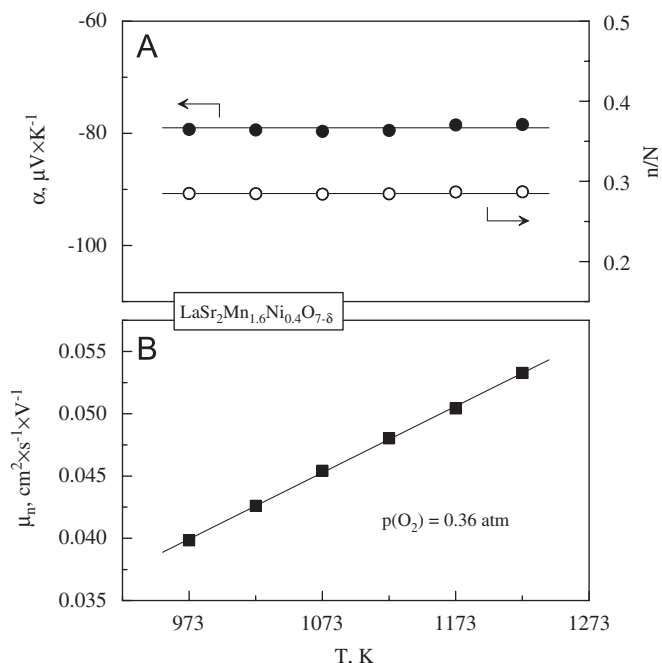


Fig. 7. Temperature dependence of the Seebeck coefficient and estimated n/N ratio (A), and electron mobility (B) of $\text{LaSr}_2\text{Mn}_{1.6}\text{Ni}_{0.4}\text{O}_{7-\delta}$ at a fixed oxygen partial pressure (see text).

The dependencies of oxygen permeation flux on $p(\text{O}_2)$ gradient (Fig. 9) deviate from the Wagner-type behavior [34] described by the classical equation:

$$j = \frac{RT}{16F^2 d} \int_{p_1}^{p_2} \frac{\sigma_e \sigma_o}{\sigma_e + \sigma_o} \partial \ln p(\text{O}_2) = \frac{RT}{16F^2} \frac{\sigma_{\text{amb}}}{d} \ln \left(\frac{p_2}{p_1} \right) \quad (2)$$

where so-called ambipolar conductivity, σ_{amb} , is determined by the partial ionic (σ_o) and electronic (σ_e) conductivities. Nonetheless, even the rough estimations of ion transference numbers by Eq. (2) unambiguously demonstrated that electronic contribution to the total conductivity of $\text{LaSr}_2\text{Mn}_{1.6}\text{Ni}_{0.4}\text{O}_{7-\delta}$ is more than 10^4 times higher than oxygen-ionic, thus showing that $\sigma_{\text{amb}} \approx \sigma_o$. The ionic transport in $\text{LaSr}_2(\text{Mn,Ni})_2\text{O}_{7-\delta}$ ceramic bulk is expected to occur via the oxygen-vacancy diffusion in $(\text{MnO}_2)_2$ planes, and should increase with reducing $p(\text{O}_2)$ due to rising oxygen deficiency. The deviation from linear permeation flux dependencies on the oxygen chemical potential gradient may be attributed, therefore, to limiting effect of the oxygen surface exchange kinetics which typically increases on reducing $p(\text{O}_2)$ [34]. Whatever the microscopic mechanisms, the oxygen permeability of $\text{LaSr}_2\text{Mn}_{1.6}\text{Ni}_{0.4}\text{O}_{7-\delta}$ (Fig. 10) is higher than that of $(\text{La,Sr})\text{MnO}_{3-\delta}$ and $(\text{La,Sr})(\text{Mn,Cr})\text{O}_{3-\delta}$ perovskites [35,36] widely used for SOFC electrodes, but is lower compared to other cathode materials, such as $(\text{Sr,Ce})\text{MnO}_{3-\delta}$ [37] or $(\text{La,Sr})(\text{Fe,Co})\text{O}_{3-\delta}$ (e.g. [35]). These relationships are primarily associated with higher oxygen-vacancy concentration in the latter perovskite compounds.

Fig. 11 illustrates typical microstructure of as-prepared porous $\text{LaSr}_2\text{Mn}_{1.6}\text{Ni}_{0.4}\text{O}_{7-\delta}$ layers applied onto $\text{La}_{10}\text{Si}_5\text{AlO}_{26.5}$ electrolyte. The electrode morphology was quite uniform, with grain sizes in the range 0.4–1.8 μm . The cathodic polarization curves at atmospheric oxygen pressure are presented in Fig. 12A. No tendencies to limiting currents are observed in the studied overpotential range. Inspection of the impedance spectra (Fig. 13) reveals the presence of at least two contributions. Taking into account the trends displayed by the oxygen permeation fluxes through

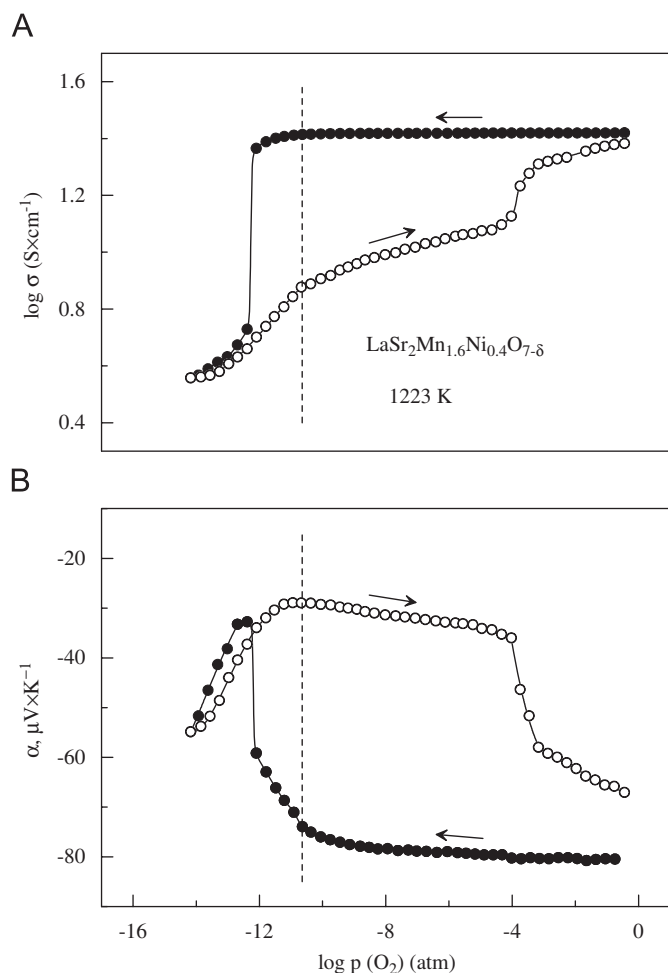


Fig. 8. Oxygen partial pressure dependence of the total conductivity (A) and Seebeck coefficient (B) of $\text{LaSr}_2\text{Mn}_{1.6}\text{Ni}_{0.4}\text{O}_{7-\delta}$ measured in a wide $p(\text{O}_2)$ range on reduction and subsequent re-oxidation, at 1223 K. The arrows indicate the direction of oxygen pressure changes. The dotted line indicates approximate phase stability limit.

Table 3

Comparison of the low- $p(\text{O}_2)$ stability limits of manganite- and nickelate-based phases

Composition	T (K)	$p(\text{O}_2)$ (atm)	Reference
$\text{LaSr}_2\text{Mn}_{1.6}\text{Ni}_{0.4}\text{O}_7$	1223	2.3×10^{-11}	This work
LaMnO_3	1273	1.2×10^{-15}	[31]
	1173	4.2×10^{-18}	
$\text{La}_{0.5}\text{Sr}_{0.5}\text{MnO}_3$	1273	6.2×10^{-13}	[31]
	1173	6.6×10^{-15}	
Mn_3O_4	1223	4.1×10^{-8}	[32]
NiO	1223	8.0×10^{-12}	[32]
La_2NiO_4	1223	6.3×10^{-14}	[33]

$\text{LaSr}_2\text{Mn}_{1.6}\text{Ni}_{0.4}\text{O}_{7-\delta}$ and numerous literature data (e.g. [38–40] and references cited), the low-frequency process should be ascribed to rate-determining oxygen exchange reaction at the electrode surface, while the high-frequency electrode contribution can be assigned to impeded ion transfer at the electrode/electrolyte interface. Generally, the electrochemical activity of $\text{LaSr}_2\text{Mn}_{1.6}\text{Ni}_{0.4}\text{O}_{7-\delta}$ is substantially lower compared to nickelate-based electrode materials, such as $\text{La}_2\text{Ni}_{0.8}\text{Cu}_{0.2}\text{O}_{4+\delta}$ [39], in correlation with oxygen permeability (Table 4). For instance, the cathodic overpotential of $\text{LaSr}_2\text{Mn}_{1.6}\text{Ni}_{0.4}\text{O}_{7-\delta}|\text{La}_{10}\text{Si}_5\text{AlO}_{26.5}$ half-

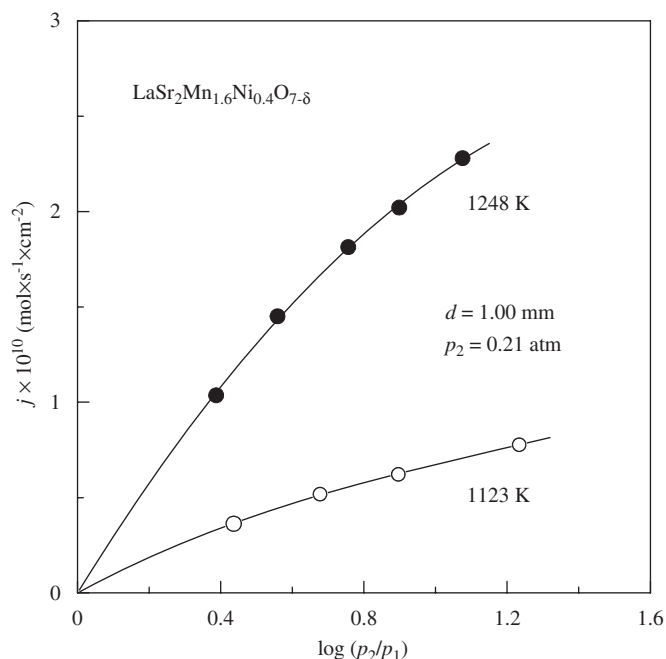


Fig. 9. Dependence of the oxygen permeation flux through a dense $\text{LaSr}_2\text{Mn}_{1.6}\text{Ni}_{0.4}\text{O}_{7-\delta}$ membrane on the oxygen partial pressure gradient at 1248 and 1123 K.

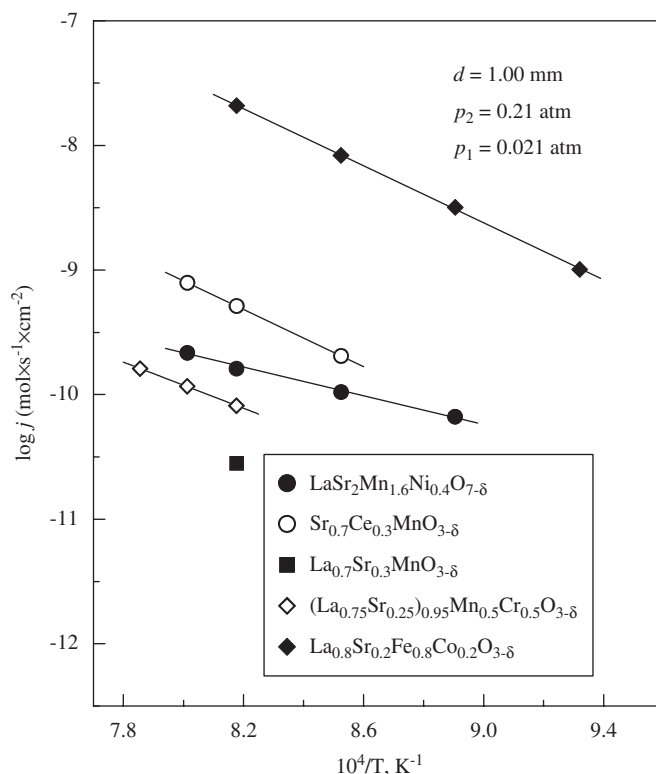


Fig. 10. Temperature dependence of the oxygen permeation fluxes through $\text{LaSr}_2\text{Mn}_{1.6}\text{Ni}_{0.4}\text{O}_{7-\delta}$ under fixed $p(\text{O}_2)$ gradient. The data on other electrode materials, including $\text{La}_{0.7}\text{Sr}_{0.3}\text{MnO}_{3-\delta}$ [35], $(\text{La}_{0.75}\text{Sr}_{0.25})_{0.95}\text{Mn}_{0.5}\text{Cr}_{0.5}\text{O}_{3-\delta}$ [36], $\text{Sr}_{0.7}\text{Ce}_{0.3}\text{MnO}_{3-\delta}$ [37] and $\text{La}_{0.8}\text{Sr}_{0.2}\text{Fe}_{0.8}\text{Co}_{0.2}\text{O}_{3-\delta}$ [35], are shown for comparison.

cell at 1073 K and current density of -40 mA/cm^2 (Fig. 12A) is about eight times larger than that of porous $\text{La}_2\text{Ni}_{0.8}\text{Cu}_{0.2}\text{O}_{4+\delta}$ applied onto the same electrolyte [39].

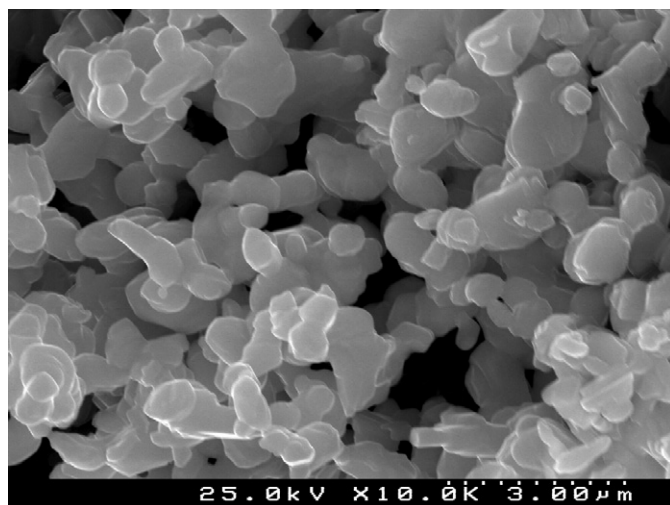


Fig. 11. Typical microstructure of $\text{LaSr}_2\text{Mn}_{1.6}\text{Ni}_{0.4}\text{O}_{7-\delta}$ electrodes.

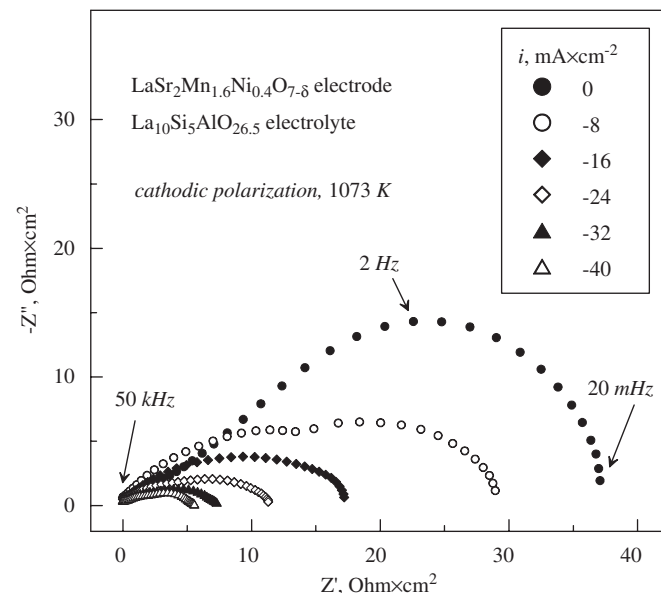


Fig. 13. Impedance spectra of $\text{LaSr}_2\text{Mn}_{1.6}\text{Ni}_{0.4}\text{O}_{7-\delta}$ electrode in contact with $\text{La}_{10}\text{Si}_5\text{AlO}_{26.5}$ electrolyte under cathodic polarization at 1073 K in air. All spectra are corrected for ohmic losses and electrode area.

Table 4

Relationships between the polarization resistance of Ni-containing oxide cathodes in contact with $\text{La}_{10}\text{Si}_5\text{AlO}_{26.5}$ under open-circuit conditions, and oxygen permeability of the electrode materials

Electrode	R_p (Ohm cm^2)			j^a (mol/s cm^2) (1123 K)	Reference
	1073 K	973 K	873 K		
$\text{LaSr}_2\text{Mn}_{1.6}\text{Ni}_{0.4}\text{O}_{7-\delta}$	24	54	109	6.6×10^{-11}	This work
$\text{La}_2\text{Ni}_{0.8}\text{Cu}_{0.2}\text{O}_{4+\delta}$	1.5	3.2	11.1	2.1×10^{-8}	[39,40]

^a $d = 1.00$ mm, $p_2 = 0.21$ atm, $p_1 = 0.021$ atm.

interdiffusion between $\text{LaSr}_2\text{Mn}_{1.6}\text{Ni}_{0.4}\text{O}_{7-\delta}$ and $\text{La}_{10}\text{Si}_5\text{AlO}_{26.5}$ electrolyte. Fig. 14 presents one example of the EDS spectra, clearly showing a substantial penetration of strontium into the surface layers of $\text{La}_{10}\text{Si}_5\text{AlO}_{26.5}$ and Mn/Ni depletion in $\text{LaSr}_2\text{Mn}_{1.6}\text{Ni}_{0.4}\text{O}_{7-\delta}$ electrode near the interface. Notice that the introduction of Sr^{2+} in the La^{3+} sites of apatite-type $\text{La}_{10}\text{Si}_5\text{AlO}_{26.5}$ lattice decreases ionic conduction due to lowering the concentration of mobile interstitial oxygen anions [20]; as a general rule, the electrode polarization resistance increases with increasing electrolyte resistivity [38]. Moreover, significant changes in the electrode composition near the electrode/electrolyte interface (Fig. 14A) should induce partial decomposition of the $n = 2$ RP phase and formation of thin interlayers with low ionic conductivity. Irrespective of the nature of ion transfer-blocking phenomena, the results indicate that relatively high polarization resistance of $\text{LaSr}_2\text{Mn}_{1.6}\text{Ni}_{0.4}\text{O}_{7-\delta}$ cathodes in contact with lanthanum silicate-based electrolyte is contributed by fast cation interdiffusion between the electrochemical cell components. As for (La,Sr) MnO_3 -based cathodes, this makes it necessary to decrease the cell fabrication and operation temperatures down to possible minimum and/or to deposit protective interlayers.

The anodic performance of $\text{LaSr}_2\text{Mn}_{1.6}\text{Ni}_{0.4}\text{O}_{7-\delta}$ at atmospheric oxygen pressure is considerably better compared to cathodic performance (Figs. 12A and B). Such behavior seems to be in agreement with the interstitial oxygen diffusion mechanism in $\text{La}_{10}\text{Si}_5\text{AlO}_{26.5}$ [19,20], where the incorporation of transition metal cations from the manganite-based electrodes should promote

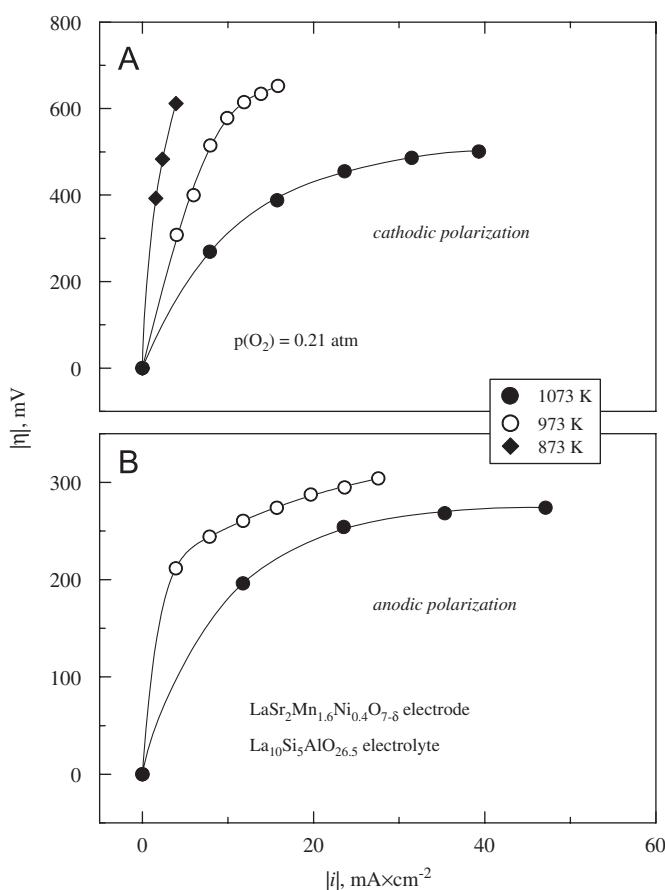


Fig. 12. Cathodic (A) and anodic (B) overpotentials of porous $\text{LaSr}_2\text{Mn}_{1.6}\text{Ni}_{0.4}\text{O}_{7-\delta}$ layer applied onto $\text{La}_{10}\text{Si}_5\text{AlO}_{26.5}$ solid electrolyte, in air.

Another important factor, which may be responsible for the relatively poor performance of $\text{LaSr}_2\text{Mn}_{1.6}\text{Ni}_{0.4}\text{O}_{7-\delta}$ cathodes, relates to partial blocking of the electrochemical reaction zone by silica due to surface diffusion, as indicated by EDS/TEM for $\text{La}_2\text{Ni}_{0.8}\text{Cu}_{0.2}\text{O}_{4+\delta}$ electrodes [39]. In the case of $\text{LaSr}_2\text{Mn}_{1.6}\text{Ni}_{0.4}\text{O}_{7-\delta}$ electrodes, however, detection of SiO_2 traces on the surface was impossible due to overlapping of the Sr and Si peaks in EDS spectra. Nevertheless, EDS analysis of the electrolyte/electrode interfaces confirmed a critical role of cation

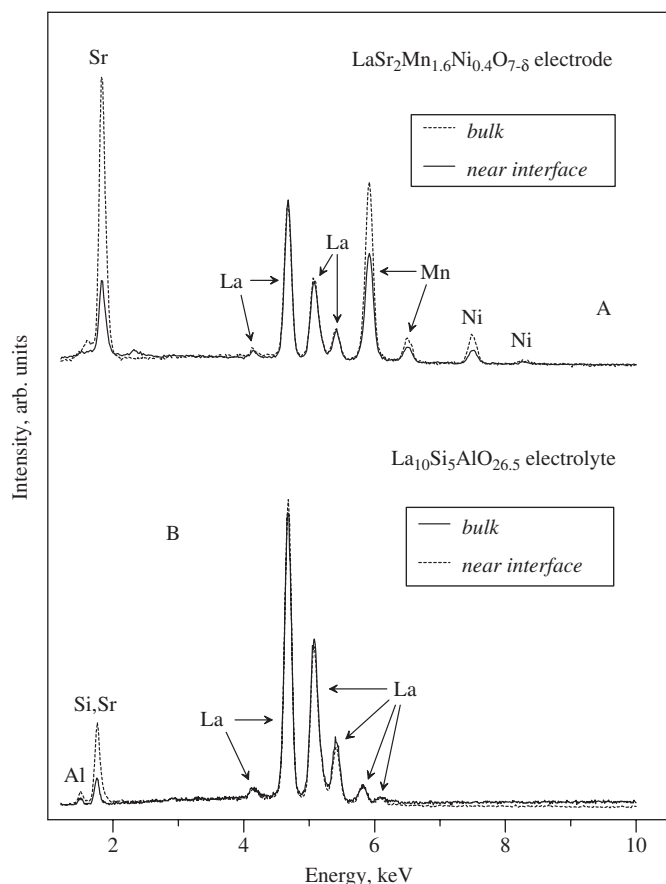


Fig. 14. Comparison of the EDS spectra of $\text{LaSr}_2\text{Mn}_{1.6}\text{Ni}_{0.4}\text{O}_{7-\delta}$ grains in the porous electrode bulk and near the electrode/electrolyte interface (A), and $\text{La}_{10}\text{Si}_5\text{AlO}_{26.5}$ in the electrolyte bulk and near interface (B).

overpotential-induced variations in the mobile anion concentration and, thus, ionic transport. Anodic polarization increases the oxygen chemical potential both in the electrode and in the interfacial electrolyte layers, where a local increase of the interstitial oxygen concentration is expected due to oxidation of the variable-valence cations introduced during electrode sintering. For the oxygen-hyperstoichiometric silicates, the interfacial processes related to oxygen transfer and diffusion should hence be facilitated under anodic polarization and hampered due to cathodic reduction.

4. Conclusions

The solubility of nickel cations in the $n=2$ RP series $\text{LaSr}_2\text{Mn}_{2-y}\text{Ni}_y\text{O}_{7-\delta}$ corresponds to $y \approx 0.5$. Doping with nickel decreases the tetragonal unit cell volume and total conductivity, and moderately increases thermal expansion. The average TECs vary in the range $(11.4\text{--}12.5) \times 10^{-6} \text{K}^{-1}$ at 300–900 K and $(13.7\text{--}14.4) \times 10^{-6} \text{K}^{-1}$ at 900–1370 K in air. The total conductivity, Seebeck coefficient and oxygen permeability of $\text{LaSr}_2\text{Mn}_{1.6}\text{Ni}_{0.4}\text{O}_{7-\delta}$ ceramics were studied in the oxygen partial pressure range 10^{-14} –0.3 atm at 600–1270 K. The electrical properties are essentially $p(\text{O}_2)$ -independent within the RP phase stability domain, reflecting almost negligible variations of the oxygen nonstoichiometry. The conductivity is predominantly n-type electronic, with oxygen-ionic contribution lower than 0.002% at 1248 K in air. The relatively low, temperature-activated mobility of electronic charge carriers suggests a small polaron conduction mechanism where nickel cations are substantially excluded from

the electron-transfer-related processes. The decomposition of $\text{LaSr}_2\text{Mn}_{1.6}\text{Ni}_{0.4}\text{O}_{7-\delta}$ in reducing conditions is observed at the oxygen partial pressures close to Ni/NiO boundary, for example $\sim 2.3 \times 10^{-11}$ atm at 1223 K. The steady-state oxygen permeability of dense $\text{LaSr}_2\text{Mn}_{1.6}\text{Ni}_{0.4}\text{O}_{7-\delta}$ membranes lies in the range typical for manganite-based electrode materials, such as perovskite-type $(\text{La,Sr})\text{MnO}_{3-\delta}$, $(\text{La,Sr})(\text{Mn,Cr})\text{O}_{3-\delta}$ and $(\text{Sr,Ce})\text{MnO}_{3-\delta}$. Irrespective of considerably high electronic conductivity and significant oxygen permeability, porous $\text{LaSr}_2\text{Mn}_{1.6}\text{Ni}_{0.4}\text{O}_{7-\delta}$ cathodes exhibit a relatively poor electrochemical performance in contact with apatite-type $\text{La}_{10}\text{Si}_5\text{AlO}_{26.5}$ solid electrolyte, which may be partly associated with strong cation interdiffusion between the cell components.

Acknowledgments

This work was supported by the FCT, Portugal (Project PTDC/CTM/64357/2006), and by the Belgian Federal Science Policy foundation.

References

- [1] Y. Moritomo, A. Asamitsu, H. Kuwahara, Y. Tokura, *Nature* 380 (1996) 141–144.
- [2] L. Malavasi, M.C. Mozatti, C. Ritter, V. Pomjakushin, C. Tealdi, C.B. Azzoni, G. Flor, *J. Phys. Chem. B* 110 (2006) 17430–17436.
- [3] X. Lan, W. Zhang, *Phys. Rev. B* 75 (2007) 134417.
- [4] W. Norimatsu, Y. Koyama, *Physica C* 463–465 (2007) 115–119.
- [5] C.N. Munnings, S.J. Skinner, G. Amow, P.S. Witfield, I.J. Davidson, *Solid State Ionics* 177 (2006) 1849–1853.
- [6] R. Seshadri, C. Martin, M. Hervieu, B. Raveau, C.N.R. Rao, *Chem. Mater.* 9 (1997) 270–277.
- [7] P.D. Battle, M.J. Rosseinsky, *Curr. Opin. Solid State Mater. Sci.* 4 (1999) 163–170.
- [8] M. Kubota, H. Fujioka, K. Hirota, K. Ohoyama, Y. Moritomo, H. Yoshizawa, Y. Endoi, *J. Phys. Soc. Japan* 69 (2000) 1606–1609.
- [9] J.F. Mitchell, D.N. Argyriou, A. Berger, K.E. Gray, R. Osborn, U. Welp, *J. Phys. Chem. B* 105 (2001) 10731–10745.
- [10] J.E. Millburn, J.F. Mitchell, D.N. Argyriou, *Chem. Commun.* (1999) 1389–1390.
- [11] J. Zhang, F. Wang, P. Zhang, Q. Yan, *J. Appl. Phys.* 86 (1999) 1604–1606.
- [12] J. Feng, P. Che, J.P. Wang, M.F. Lu, J.F. Liu, X.Q. Cao, J. Meng, *J. Alloys Compd.* 397 (2005) 220–225.
- [13] M. Matsukawa, M. Chiba, E. Kikuchi, R. Suryanarayanan, M. Apostu, S. Nimori, K. Sugimoto, N. Kobayashi, *Phys. Rev. B* 72 (2005) 224422.
- [14] R.L. Zhang, W.H. Song, Y.Q. Ma, J. Yang, B.C. Zhao, Z.G. Sheng, J.M. Dai, Y.P. Sun, *Phys. Rev. B* 70 (2004) 224418.
- [15] H. Zhu, X.J. Xu, L. Pi, Y.H. Zhang, *Phys. Rev. B* 62 (2000) 6754–6760.
- [16] G. Amow, S.J. Skinner, *J. Solid State Electrochem.* 10 (2006) 538–546.
- [17] M.A. Bobina, N.A. Yakovleva, L.Ya. Gavrilova, V.A. Cherepanov, *Russ. J. Phys. Chem.* 78 (2004) 1340–1343.
- [18] A.N. Demina, V.A. Cherepanov, A.N. Petrov, M.V. Klokova, *Inorg. Mater.* 41 (2005) 736–742.
- [19] A.L. Shaula, V.V. Kharton, F.M.B. Marques, *J. Solid State Chem.* 178 (2005) 2050–2061.
- [20] V.V. Kharton, F.M.B. Marques, A. Atkinson, *Solid State Ionics* 174 (2004) 135–149.
- [21] L.A. Chick, L.R. Pederson, G.D. Maupin, J.L. Bates, L.E. Thomas, G.L. Exarhos, *Mater. Lett.* 10 (1990) 6–12.
- [22] M.V. Patrakeev, E.B. Mitberg, A.A. Lakhtin, I.A. Leonidov, V.L. Kozhevnikov, V.V. Kharton, M. Avdeev, F.M.B. Marques, *J. Solid State Chem.* 167 (2002) 203–213.
- [23] V.V. Kharton, V.N. Tikhonovich, L. Shuangbao, E.N. Naumovich, A.V. Kovalevsky, A.P. Viskup, I.A. Basmakov, A.A. Yaremchenko, *J. Electrochem. Soc.* 145 (1998) 1363–1374.
- [24] J. Mizusaki, H. Tagawa, K. Isobe, M. Tajika, I. Koshiro, H. Maruyama, K. Hirano, *J. Electrochem. Soc.* 141 (1994) 1674–1683.
- [25] V.V. Kharton, A.A. Yaremchenko, E.N. Naumovich, *J. Solid State Electrochem.* 3 (1999) 303–326.
- [26] M. Al Daroukh, V.V. Vashook, H. Ullmann, F. Tietz, I.A. Raj, *Solid State Ionics* 158 (2003) 141–150.
- [27] R. Raffaele, H.U. Anderson, D.M. Sparlin, P.E. Parris, *Phys. Rev. B* (1991) 7991–7999.
- [28] S. Kirkpatrick, *Rev. Mod. Phys.* 45 (1973) 574–588.
- [29] P. Kofstad, *Nonstoichiometry, Diffusion and Electrical Conductivity in Binary Metal Oxides*, Wiley-Interscience, New York, 1972.
- [30] D.O. Bannikov, V.A. Cherepanov, *J. Solid State Chem.* 179 (2006) 2721–2727.

- [31] J. Mizusaki, N. Mori, H. Takai, Y. Yonemura, H. Minamiue, H. Tagawa, M. Dokiya, H. Inaba, K. Naraya, T. Sasamoto, T. Hashimoto, *Solid State Ionics* 129 (2000) 163–177.
- [32] G.G. Charette, S.N. Flengas, *J. Electrochem. Soc.* 115 (1968) 796–804.
- [33] D.E. Rice, D.J. Buttrey, *J. Solid State Chem.* 105 (1993) 197–210.
- [34] H.J.M. Bouwmeester, A.J. Burgraaf, in: A.J. Burgraaf, L. Cot (Eds.), *Fundamentals of Inorganic Membrane Science and Technology*, Elsevier, Amsterdam, 1996, p. 435.
- [35] V.V. Kharton, A.V. Kovalevsky, A.P. Viskup, A.L. Shaula, F.M. Figueiredo, E.N. Naumovich, F.M.B. Marques, *Solid State Ionics* 160 (2003) 247–258.
- [36] V.V. Kharton, E.V. Tsipis, I.P. Marozau, A.P. Viskup, J.R. Frade, J.T.S. Irvine, *Solid State Ionics* 178 (2007) 101–113.
- [37] V.V. Kharton, A.P. Viskup, I.P. Marozau, E.N. Naumovich, *Mater. Lett.* 57 (2003) 3017–3021.
- [38] T. Kenjo, Y. Kanehira, *Solid State Ionics* 148 (2002) 1–14.
- [39] E.V. Tsipis, V.V. Kharton, J.R. Frade, *Electrochim. Acta* 52 (2007) 4428–4435.
- [40] V.V. Kharton, E.V. Tsipis, A.A. Yaremchenko, J.R. Frade, *Solid State Ionics* 166 (2004) 327–337.